


Optimal Design of a Highly Self-Adaptive Gripper with Multi-Phalange Compliant Fingers for Grasping Irregularly Shaped Objects

Chih-Hsing Liu , Member, IEEE, Sy-Yeu Yang, and Yi-Chieh Shih

Abstract—The development of a robotic gripper for handling objects of various sizes, shapes, weights, and degrees of hardness is a challenging problem in the field of robotics. In order to design a highly self-adaptive gripper capable of conforming to a wide range of objects, this article presents an innovative topology-optimized design of a compliant finger consisting of several multi-material phalanges connected by flexure hinges. The prototype was produced by means of a metamaterial approach, which utilizes 3D-printed infill structures (periodic cells) with different infill densities to represent regions with different equivalent mechanical properties. Adaptability tests were conducted to demonstrate the effectiveness of the proposed design in grasping circular, rectangular, trapezoidal, and concave objects. The results were compared with those of the fingers with single infill densities and a commercially available Festo MultiChoiceGripper, which features a Fin Ray structure. The total contact length between the fingers and the grasped object was used as a measure of the grippers' adaptability. The test results demonstrate that this novel self-adaptive gripper is comparatively highly adaptable for grasping irregularly shaped objects and is able to carry a maximum payload of 6.76 kg.

Index Terms—Adaptive gripper, compliant finger, compliant gripper, multi-material, soft robot, topology optimization.

I. INTRODUCTION

THE development of robotic grippers for the purpose of handling irregularly shaped objects has drawn considerable attention in recent years [1], [2], [3], [4], [5], [6], [7]. A robotic gripper is typically the only interface between a robot and its working environment. Therefore, the overall performance of the robot largely depends on the design of its gripper [8]. A dexterous robotic gripper typically has multiple degrees of freedom and requires multiple actuators to execute planned movements. As the number of actuators increases, so do certain aspects of the design, such as the control complexity, the overall size, and the cost. Designing underactuated mechanisms [9] is crucial for minimizing the use of actuators. In order to achieve this goal,

Manuscript received 14 April 2023; accepted 25 August 2023. Date of publication 11 September 2023; date of current version 19 September 2023. This letter was recommended for publication by Associate Editor H. Stuart and Editor Y. Park upon evaluation of the reviewers' comments. This work was supported by the Ministry of Science and Technology of Taiwan under Grants MOST 110-2628-E-006-004 and MOST 111-2628-E-006-001-MY2. (Corresponding author: Chih-Hsing Liu.)

The authors are with the Department of Mechanical Engineering, National Cheng Kung University, Tainan 701, Taiwan (e-mail: chliu@mail.ncku.edu.tw; mrsimple851024@gmail.com; jasonimshih@gmail.com).

Digital Object Identifier 10.1109/LRA.2023.3313877

passive elastic elements are currently being used [10], such as preloaded springs [9] and flexure hinges [11], [12], [13], [14].

The latest advances in soft robotics, materials science, and stretchable electronics have led to rapid progress in the development of soft grippers [1]. Compared with rigid robots, soft robots have many advantages, including safer human-robot interactions and adaptive behaviors suitable for handling unknown objects in complex environments [15]. Soft grippers have been used in wide range of applications, from underwater grasping [16], [17] to food handling [7], [18], [19] to poultry processing [20], [21]. Designing a universal gripper capable of grasping various objects is a challenging problem in the field of robotics [5], especially when properties of the objects such as size, shape, weight, and degree of hardness vary. In addition, appropriate damping and friction models [21], [22], [23] may be required to analyze the dynamic responses of flexible systems.

In order to develop a gripper that can adapt to such a variety of objects, bioinspired concepts [24], [25], [26] and optimization algorithms [27], [28], [29], [30], [31], [32], [33], [34] are currently being explored. For example, grippers with a Fin Ray structure [25], [26] are nature-inspired designs intended to conform to a wide range of objects while grasping. Compliant grippers that are synthesized using topology optimization algorithms while taking into consideration the presence of multiple output ports [3], [4], [32] have been developed to be suitable for grasping unknown objects.

Topology optimization is a numerical method that can be used to optimize the material distribution in a given design domain, and it has been used to synthesize various compliant fingers and grippers [3], [4], [27], [28], [29], [30], [31], [32], [33], [34]. For example, Chen et al. [29] developed a cable-driven, three-fingered soft robotic gripper with compliant fingers which were synthesized by applying a level-set topology optimization algorithm. Their experimental results showed that their 3D-printed design, made of a thermoplastic elastomer (TPE), was able to grip objects that weighed up to 1 kg. In another study, Zhang et al. [31] designed a three-fingered, multi-material soft pneumatic gripper using a density-based topology optimization algorithm. Its fingers were made of silicone rubber and TPE and had the ability to grip objects that weighed up to 168 g at a supply pressure of 70 kPa.

The use of soft materials generally reduces the maximum load capacity of a gripper. In order to increase the maximum payload, several motor-driven, two-fingered, topologically optimized compliant grippers [3], [32], [34] have been developed. These grippers were synthesized under a single design domain, taking into account different objective functions and boundary

conditions. These designs were made of either TPE [3], [34] or silicone rubber [32], and their maximum payloads ranged between 2 and 3 kg. In addition, multi-material designs [31], [34] have been developed in order to increase the adaptability of the grippers and achieve better performance. In our previous study [34], we developed a multi-material design produced by means of a metamaterial approach [35], [36], which uses 3D-printed infill structures with different infill densities (or infill percentages) to represent regions with different equivalent mechanical properties. The results demonstrated that, compared with a single-material compliant finger with the same volume and weight, the bi-material compliant finger was a better design for reducing the driving force and increasing the output displacement.

Motivated by the need to design a self-adaptive gripper that can automatically conform to irregularly shaped objects, this article presents an innovative design for a compliant finger consisting of multiple topologically optimized multi-material phalanges connected by flexure hinges. A new three-material model and corresponding element sensitivities for topology optimization are introduced in this study. The fingers are 3D-printed using TPE, with varying infill densities across different regions of each finger. A prototype of a two-fingered gripper is developed, as the two-fingered configuration is widely used in the industry. Finally, the results of adaptability and payload tests are compared with those obtained from grippers 3D-printed with single infill densities, as well as with a commercially used Festo MultiChoiceGripper [37] that features a Fin Ray structure.

II. MULTI-PHALANGE COMPLIANT FINGER

Unlike previous studies [3], [4], [32], [34] that synthesized compliant fingers under the condition of a single design domain, this study divided the compliant finger into multiple phalanges connected by flexure hinges. The schematic drawing of the proposed two-fingered compliant gripper is shown in Fig. 1, with Fig. 1(a) and (b) demonstrating the mechanism in its initial state and while grasping, respectively. Two identical multi-phalange compliant fingers were installed on the driving module of the gripper, with a distance of 60 mm between them in the initial state. The driving module consisted of a main structure with two fixed stages connected by two structural rods and a linear stage. It was driven by a stepper motor connected to a timing belt pulley and a threaded rod. The input port of each finger was installed on the linear stage, whereas the fixed port was installed on the lower fixed stage. As illustrated in Fig. 1(b), when the linear stage was moved toward the lower fixed stage, both multi-phalange compliant fingers bent inward elastically in order to grip an object. As shown in Fig. 1(c), the compliant finger structure was divided into five design domains with one drive link and the remaining four domains corresponding to finger phalanges. Each design domain was optimized independently using a topology optimization method.

The drive link is a compliant mechanism with the function of pushing the finger phalanges. A displacement input was applied at the lower right corner of the drive link (the input port shown in Fig. 1(c)) through the motor-driven linear stage, while the lower left corner of the drive link (the fixed port) was fixed. In addition, based on existing designs that incorporate flexure hinges in the design of compliant mechanisms [11], [12], flexure hinges were used to connect adjacent finger phalanges in this study. A multi-material topology optimization method was used

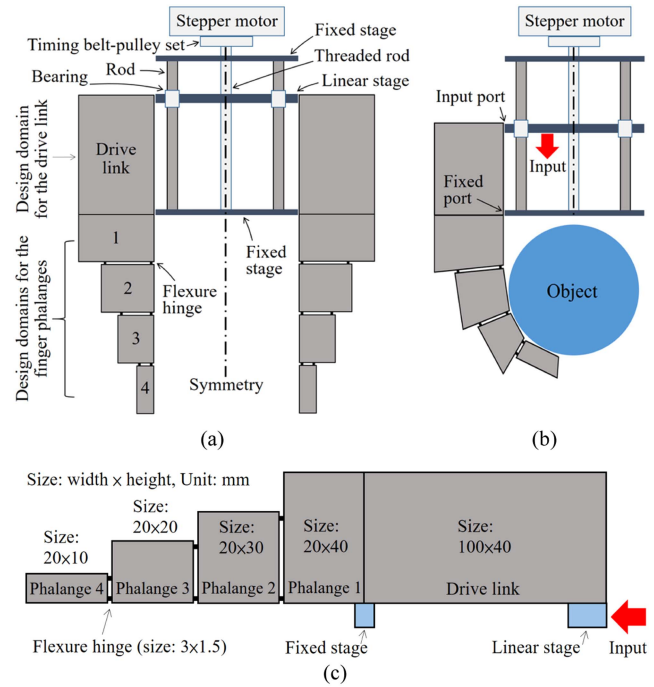


Fig. 1. Schematic drawing of the two-fingered gripper with multi-phalange compliant fingers. (a) The two-fingered gripper in its initial state. (b) A single finger grasping. (c) The design domains of the multi-phalange finger.

to identify the optimal material distribution within each design domain through an iterative procedure.

The loading conditions for each design domain were presented in Fig. 2, where the dark regions of the four phalanges represented the gripping surface of the finger which must be filled with material; f_{in} was a dummy input force; f_{out} was a dummy output force; and k represented the stiffness of the numerical spring placed at the input and output ports. In Fig. 2(a), the input force in the design domain of the drive link corresponded to the input from the linear stage at the input port (Port 1), while the fixed port was mounted on the lower fixed stage, as shown in Fig. 1. The target output port (Port 2) of the drive link was located at the upper left corner of the design domain. It provided an input to finger phalange 1, as illustrated in Fig. 2(b). Finger phalange 1 had two target output ports (Ports 3 and 4). Port 3 was the expected contact location with the object, whereas Port 4 was the location where the output force of finger phalange 1 was transferred to finger phalange 2 as an input force. The loading conditions for phalanges 2 and 3, which were shown in Figs. 2(c) and (d), respectively, were similar to the loading conditions for finger phalange 1. The output force at Port 8 of finger phalange 3 was transferred to finger phalange 4 as an input force, as shown in Fig. 2(e), with the target output port (Port 9) located at the lower left corner of the design domain, which corresponded to the fingertip of the compliant finger.

III. MULTI-MATERIAL TOPOLOGY OPTIMIZATION METHOD

A multi-material topology optimization method that can solve three-material problems is proposed with the aim of synthesizing the optimal material distribution of the multi-phalange finger shown in Fig. 2. The elastic modulus of an element for a single-material topology optimization problem [38] can be formulated

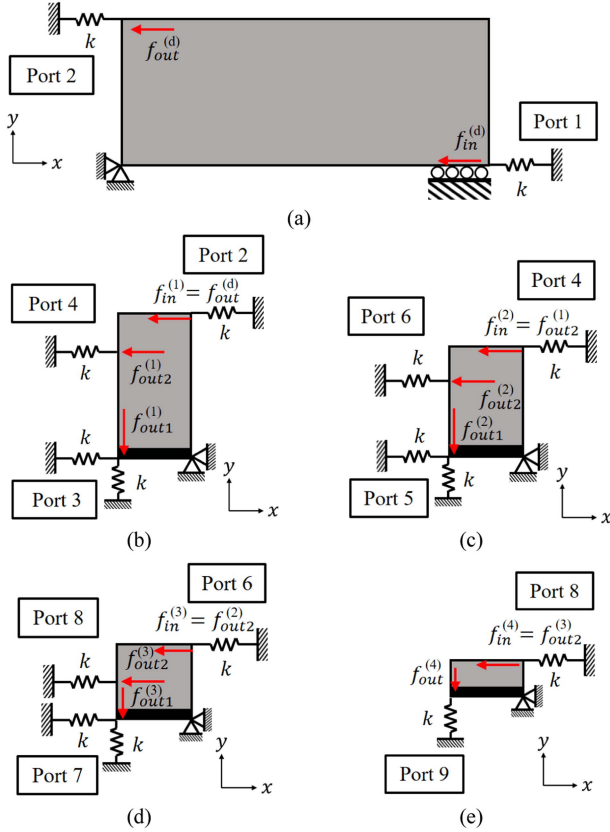


Fig. 2. Loading conditions for each design domain of the multi-phalange compliant finger. (a) Drive link. (b) Phalange 1. (c) Phalange 2. (d) Phalange 3. (e) Phalange 4.

as

$$E_i = E_{\min} + \bar{\rho}_i^p (E_o - E_{\min}) \quad (1)$$

where E_i is the elastic modulus of the i^{th} element; E_{\min} is the elastic modulus of a void element that has a small positive value close to zero; $\bar{\rho}_i$ is the projected density of the i^{th} element after projection [39]; p is the penalty parameter; and E_o is the elastic modulus of the original material.

For a two-material problem [34], the elastic modulus can be formulated as

$$E_i = E_{\min} + \bar{\rho}_{1i}^p [\bar{\rho}_{2i}^p (E_1 - E_{\min}) + (1 - \bar{\rho}_{2i}^p) (E_2 - E_{\min})] \quad (2)$$

where E_1 and E_2 are the elastic moduli of materials 1 and 2, respectively; and $\bar{\rho}_{1i}$ and $\bar{\rho}_{2i}$ are the first and second projected densities of the i^{th} element, respectively.

Based on (2), the elastic modulus for a three-material problem can be formulated as

$$E_i = (1 - \bar{\rho}_{1i}^p) E_{\min} + \bar{\rho}_{1i}^p (1 - \bar{\rho}_{2i}^p) E_3 + \bar{\rho}_{1i}^p \bar{\rho}_{2i}^p (1 - \bar{\rho}_{3i}^p) E_2 + \bar{\rho}_{1i}^p \bar{\rho}_{2i}^p \bar{\rho}_{3i}^p E_1; \quad E_1 > E_2 > E_3 \quad (3)$$

where E_3 is the elastic modulus of material 3; and $\bar{\rho}_{3i}$ is the third projected density of the i^{th} element. The three density variables, $\bar{\rho}_{1i}$, $\bar{\rho}_{2i}$, and $\bar{\rho}_{3i}$, determine the material type of the i^{th} element. The relationships among the density variables and the material types are summarized in Table I. For example, if the three density variables of the i^{th} element are all equal to 1, the resulting elastic modulus is E_1 , according to (3).

TABLE I

RELATIONSHIPS AMONG THE DENSITY VARIABLES AND MATERIAL TYPES

$\bar{\rho}_{1i}$	$\bar{\rho}_{2i}$	$\bar{\rho}_{3i}$	E_i
1	1	1	E_1
1	1	0	E_2
1	0	any	E_3
0	any	any	E_{\min}

The projected density variables shown in (3) can be calculated using the following projection scheme [39]:

$$\bar{\rho}_i = \frac{\tanh(\beta\eta) + \tanh(\beta(\bar{\rho}_i - \eta))}{\tanh(\beta\eta) + \tanh(\beta(1 - \eta))} \quad (4)$$

where β is the projection parameter; η is the threshold value; and $\bar{\rho}_i$ is the filtered density of the i^{th} element that can be obtained using the following density filter [38]:

$$\tilde{\rho}_i = \frac{\sum_{j \in N_r} w_{ij} v_j \rho_j}{\sum_{j \in N_r} w_{ij} v_j}; \quad w_{ij} = r - r_{ij} \quad (5)$$

where N_r is the neighborhood set of elements lying within the filtering radius r of the i^{th} element; w_{ij} is the weighting factor; v_j is the volume of the element j ; ρ_j is the density of element j that can be varied from 0 to 1 in small increments; and r_{ij} is the distance between the neighboring element j and the i^{th} element.

For a single element, the sensitivity of the mutual potential energy with respect to the projected density is [34]

$$\frac{\partial MPE}{\partial \bar{\rho}_i} = -\mathbf{u}_{1i}^T \frac{\partial \mathbf{k}_i}{\partial \bar{\rho}_i} \mathbf{u}_{2i} \quad (6)$$

where MPE stands for the mutual potential energy; \mathbf{u}_{1i} and \mathbf{u}_{2i} are the nodal displacement vectors of the i^{th} element corresponding to the input and output force vectors, respectively; and \mathbf{k}_i is the stiffness matrix of the i^{th} element.

The stiffness matrix of an element is linearly proportional to the elastic modulus of the i^{th} element:

$$\mathbf{k}_i = E_i \mathbf{k}_0 \quad (7)$$

where \mathbf{k}_0 is the stiffness matrix of the element with an elastic modulus of 1; and E_i is defined in (1), (2), and (3) based on whether a one-material, two-material, or three-material condition is being used, respectively.

The sensitivity of the mutual potential energy with respect to the element density can be written as the following equation based on (4), (5), (6) and (7):

$$\begin{aligned} \alpha_i &= \frac{\partial MPE}{\partial \bar{\rho}_i} = \sum_{j \in N_{r,i}} \frac{\partial MPE}{\partial \bar{\rho}_j} \frac{\partial \bar{\rho}_j}{\partial \bar{\rho}_i} \\ &= \sum_{j \in N_{r,i}} -\frac{\partial E_i}{\partial \bar{\rho}_i} \mathbf{u}_{1i}^T \mathbf{k}_0 \mathbf{u}_{2i} \frac{\partial \bar{\rho}_j}{\partial \bar{\rho}_i} \frac{\partial \bar{\rho}_j}{\partial \rho_i} \end{aligned} \quad (8)$$

In this study, the three-material model is used. Substituting (3) into (8) yields the element sensitivities for the three-material condition, where the derivatives of the elastic modulus with respect to the first, second, and third projected densities of the i^{th} element are

$$\begin{aligned} \frac{\partial E_i}{\partial \bar{\rho}_{1i}} &= p \bar{\rho}_{1i}^{p-1} [-E_{\min} + (1 - \bar{\rho}_{2i}^p) E_3 + \bar{\rho}_{2i}^p (1 - \bar{\rho}_{3i}^p) E_2 \\ &\quad + \bar{\rho}_{2i}^p \bar{\rho}_{3i}^p E_1] \end{aligned} \quad (9)$$

$$\frac{\partial E_i}{\partial \rho_{2i}^p} = p \rho_{1i}^p \rho_{2i}^{p-1} [-E_3 + (1 - \rho_{3i}^p) E_2 + \rho_{3i}^p E_1] \quad (10)$$

$$\frac{\partial E_i}{\partial \rho_{3i}^p} = p \rho_{1i}^p \rho_{2i}^p \rho_{3i}^{p-1} (-E_2 + E_1) \quad (11)$$

The numerical calculations are performed in the Matlab environment. After the element sensitivities have been obtained, the design variables are updated based on the values of sensitivities using the method of moving asymptotes (MMA) [40], which converts the *MPE* maximization problem into a negative *MPE* minimization problem in practice until convergence has been achieved under a volume fraction constraint (i.e., the ratio of the target volume of the compliant mechanism to the total volume of the design domain). In addition, a robust formulation based on eroded, intermediate, and dilated projections [41] is used in order to obtain an optimal design that takes into consideration the manufacturing tolerance.

IV. TOPOLOGY OPTIMIZATION DESIGN

The multi-material topology optimization method discussed in Section III is used to identify the optimal material distribution of the multi-phalange finger. The optimization problem for synthesizing the drive link and phalange 4, as shown in Fig. 2, is intended to maximize the mutual potential energy, which can be formulated as follows:

$$MPE = \mathbf{U}_2^T \mathbf{K} \mathbf{U}_1 \quad (12)$$

where \mathbf{K} is the global stiffness matrix of the design domain, which can be formed by assembling element matrices by means of the finite element method; \mathbf{U}_1 is the global displacement vector corresponding to the global input force vector \mathbf{F}_1 when only the input force f_{in} acts on the input port; and \mathbf{U}_2 is the global displacement vector corresponding to the output force vector \mathbf{F}_2 when only the output force f_{out} acts on the output port. The displacement vectors in (12) can be obtained based on the following equations:

$$\mathbf{K} \mathbf{U}_1 = \mathbf{F}_1; \mathbf{K} \mathbf{U}_2 = \mathbf{F}_2 \quad (13)$$

Maximizing the mutual potential energy resulting from two different sets of loading enables a design to maximize its nodal displacement at the output port while applying the input force at the input port. In addition, greater output displacement allows the finger to have a better chance of conforming to the target object. To synthesize compliant mechanisms with two output ports, such as phalanges 1, 2, and 3, the objective function of the optimization problem aims to maximize the overall mutual potential energy. By adding up the mutual potential energy for each output load (f_{out1} and f_{out2}) yields the overall mutual potential energy:

$$MPE_{sum} = MPE_1 + MPE_2 \quad (14)$$

The three-material topology optimization method was used to synthesize the optimal material distribution of each design domain shown in Fig. 2. The iterative results for the values of objective functions and the material layouts derived during some iterations are presented in Fig. 3, with (a)–(e) corresponding to the topology optimization results for the drive link and phalanges 1, 2, 3, and 4, respectively. The three colors represent the three materials for which the value of the elastic modulus differs. Due to the use of the projection method [39], the objective function value showed a noticeable decrease approximately every 50 iterations until convergence. The optimized results for each

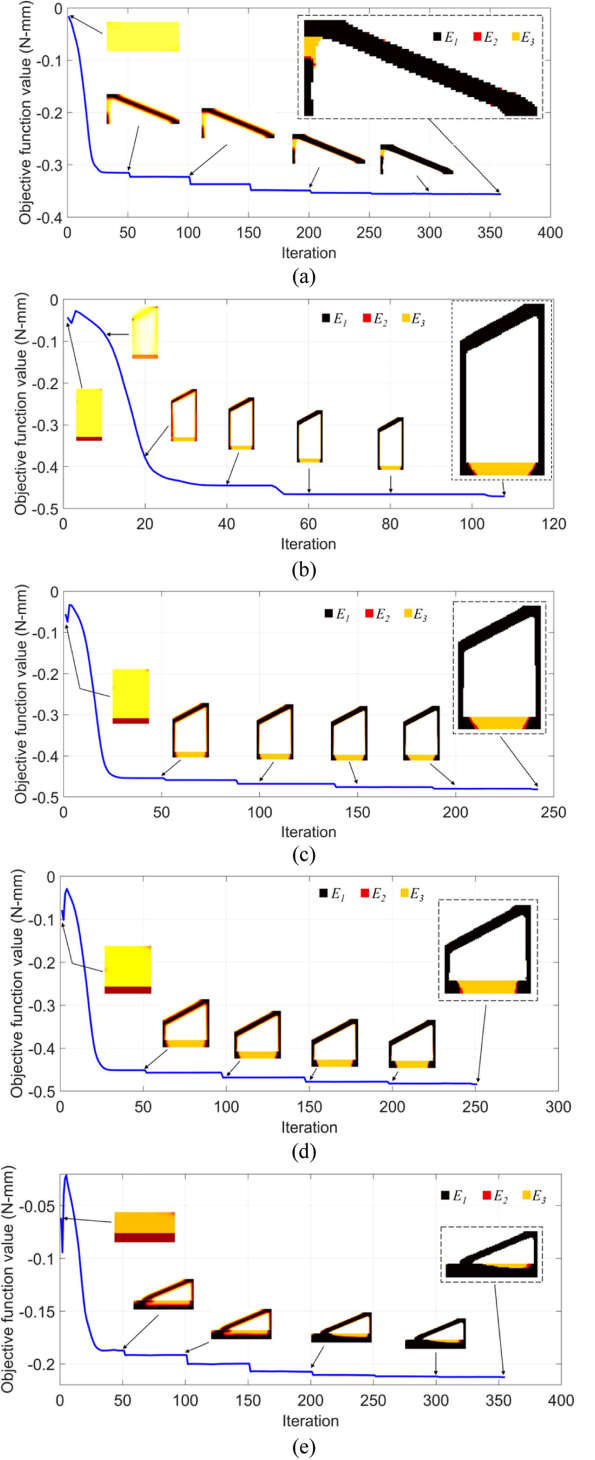


Fig. 3. Iterative results for the objective function values and the material distributions. (a) Drive link. (b) Phalange 1. (c) Phalange 2. (d) Phalange 3. (e) Phalange 4.

design domain are presented in Fig. 4(a), and the numerical parameters used in the topology optimization are summarized in Table II.

From Fig. 4(a), it can be seen that material E_2 was mainly present in the interface between material E_1 and material E_3 and appeared slightly at the boundary of the drive link. Since the proportion of material E_2 was quite low after optimization, it was

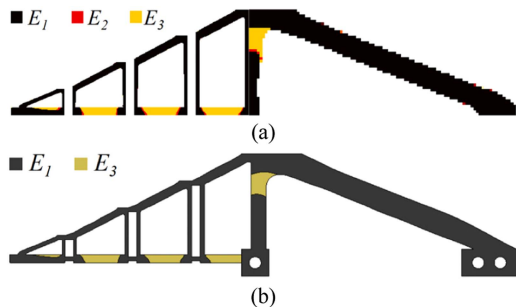


Fig. 4. Multi-material topology optimization of the multi-phalange compliant finger. (a) Topology optimization results. (b) Design model of the finger.

TABLE II
NUMERICAL PARAMETERS USED IN THE TOPOLOGY OPTIMIZATION

Parameter	Value
Element size: drive link	1 mm
Element size: finger phalanges 1 and 2	0.25 mm
Element size: finger phalanges 3 and 4	0.125 mm
Elastic modulus: 100% infill (E_1)	34.95 MPa [42]
Elastic modulus: 80% infill (E_2)	26.39 MPa [42]
Elastic modulus: 40% infill (E_3)	14.46 MPa [42]
Elastic modulus: void element (E_{min})	10^{-9} MPa
Poisson's ratio	0.45
Volume fraction: finger segments	0.22
Volume fraction: drive link	0.25
Filtering radius (r)	$5 \times$ element size
Penalty parameter (p)	3
Projection parameter (β)	1~512
Threshold values (η)	0.3, 0.5, 0.7
Dummy input and output forces	1 N
Spring stiffness (k)	1 N/mm

neither necessary nor practical to build a prototype that included material E_2 . The design model of the compliant finger structure, which is presented in Fig. 4(b), was based on the topology optimization results shown in Fig. 4(a), and thus incorporated only materials E_1 and E_3 (since the proportion of material E_2 was quite low after optimization). The four phalanges were connected by the flexure hinges, and mounting holes were added at the input and fixed ports of the finger (see Fig. 1(b)).

V. FINGER PROTOTYPES AND EXPERIMENTAL RESULTS

A prototype of the design for the multi-material compliant finger shown in Fig. 4(b) was produced by means of 3D printing using the commercial TPE filament, FilasticTM, manufactured by BotFeeder. As summarized in Table II, the infill densities of 100% and 40% corresponded to materials with equivalent elastic moduli of 34.95 MPa and 14.46 MPa, respectively [42]. A Raise3D printer was used to produce prototypes with a uniform thickness of 20 mm and a rectilinear infill pattern. Fig. 5(a) shows the prototype of the multi-infill density finger, which weighs 36.73 g. For the purpose of comparison, prototypes of the multi-material design shown in Fig. 4(b) were also produced using single infill densities of 100%, 90%, and 40%, respectively. The infill densities of 100% and 90% were chosen because the weight of the multi-infill density finger fell between that of the prototypes with single 100% and 90% infill densities, which weighed 38.39 g and 35.62 g, respectively. The weight of the 40% finger was 20.82 g. Fig. 5(b) and (c) show the compliant fingers printed with an infill density of 100% and 40%, respectively. The appearance of the finger printed with a 90% infill density is nearly identical to that of the finger printed

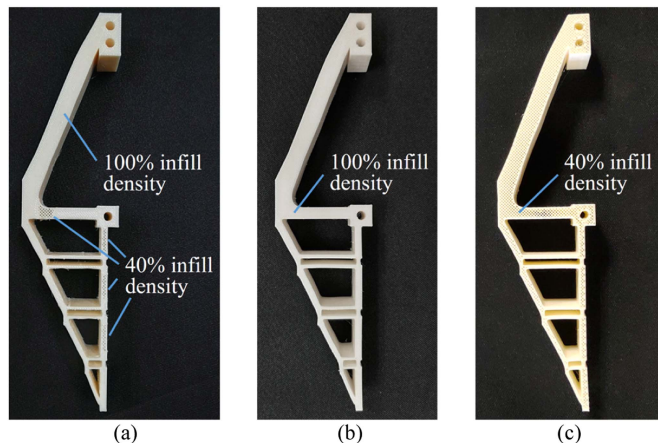


Fig. 5. 3D-printed prototypes. (a) Multi-infill density finger: the multi-material design in Fig. 4(b) achieved by varying the infill densities (40% and 100%). (b) The compliant finger printed with an infill density of 100%. (c) The compliant finger printed with an infill density of 40%.

TABLE III
MANUFACTURING PARAMETERS FOR THE 3D-PRINTED COMPLIANT FINGERS

Parameter	Value
Filament	Filastic TM TPE
Extrusion width	0.4 mm
Layer height	0.2 mm
Perimeter shell	1
Printing speed	60 mm/s
Extruder temperature	225°C
Heated bed temperature	50°C
Infill pattern	Rectilinear

with a 100% infill density. The manufacturing parameters for these fingers are summarized in Table III.

The experimental setup for measuring the relationships between the input displacement and the input force, as well as the input displacement and the output displacement (at the fingertip), is shown in Fig. 6(a). The input displacement was determined by the linear motion of the linear stage, and a force gauge was used to measure the input force required to achieve a given input displacement. Fig. 6(a) and (c) show the deformed contours of the finger from both the experimental procedure and the finite element analysis (FEA) perspectives, corresponding to input displacement values of 10 mm and 20 mm, respectively. The FEA model shown in Fig. 6 was developed using the commercially available FEA software LS-DYNA. The experimental and numerical results show good agreement.

Fig. 7(a) shows the curves representing the relationship between the input displacement and the output displacement for the multi-infill density finger, as well as the fingers printed with single infill densities of 100%, 90%, and 40%. During the experiment, the input displacement was measured at the input port of the finger, while the output displacement was measured at the fingertip. A positive input displacement referred to the movement of the linear stage towards the fixed stage (see Fig. 6(a)), whereas a negative input displacement referred to movement in the opposite direction. Fig. 7(a) shows that the output displacement of the multi-infill density finger was about 9% larger, on average, than that of the fingers printed with single infill densities. When the input displacement was 30 mm, the output displacement of the multi-infill density finger was about

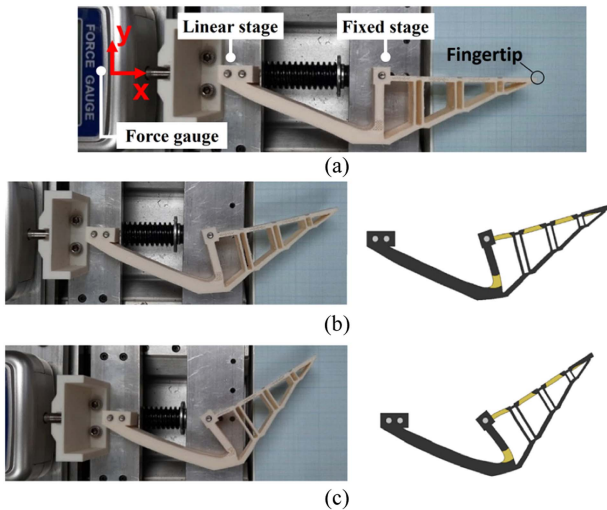


Fig. 6. Experimental and simulated results for the finger deformation tests. (a) Experimental setup for measuring the relationships between the input displacement and the input force and between the input displacement and the output displacement (at the fingertip) curve. (b) Input displacement = 10 mm. (c) Input displacement = 20 mm.

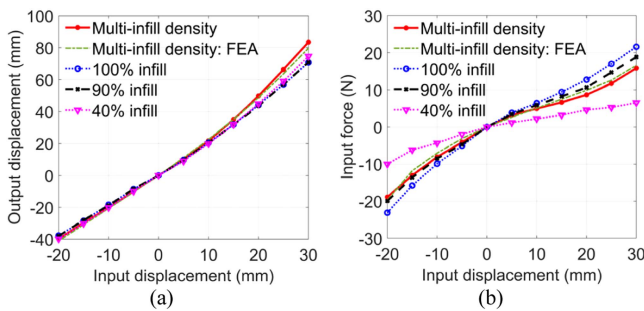


Fig. 7. Comparison of the results. (a) Input displacement versus output displacement curves. (b) Input displacement versus input force curves.

1.16 times that of the other fingers. Fig. 7(a) also shows the simulation results for the multi-material design, which are in good agreement with the experimental results.

The curves representing the relationship between the input displacement and the input force for these fingers are shown in Fig. 7(b). It can be seen that the finger printed with a single 40% infill density required less input force, as its weight was roughly 56% of the other fingers. However, it exhibited insufficient overall stiffness, making it prone to excessive deformation and buckling when gripping objects. For the other fingers with similar weights, the multi-infill density finger required less input force compared to the two fingers printed with single infill densities of 90% and 100%. The input force required for the multi-infill density finger was 12.4% and 23.2% lower, on average, than that of the fingers with the single infill densities of 90% and 100%, respectively. In addition, Fig. 7(b) also presents the simulation result for the multi-material design, which is in good agreement with the experimental data.

VI. GRIPPER PROTOTYPES AND EXPERIMENTAL RESULTS

Fig. 8 shows images of the two-fingered gripper with two identical multi-phalange, multi-infill density, compliant fingers

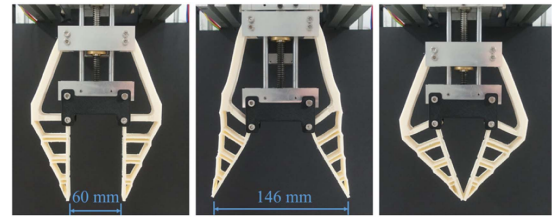


Fig. 8. Initial state, open mode, and closed mode of the soft robotic gripper with two identical multi-phalange, multi-infill density, and compliant fingers.

TABLE IV
SUMMARY OF THE TESTING RESULTS OF THE TOTAL CONTACT LENGTH RATIO FOR DIFFERENT GRIPPERS BASED ON FESTO'S DESIGN

Object \ Gripper	Multi-infill density	100% infill	Festo (Fin Ray)
Circular object	1.17	1.06	1
Rectangular object	9.65	6.45	1
Trapezoidal object	28.85	27.80	1
Concave object	20.45	2.83	1
Average	15.03	9.54	1

in the initial state, the open mode, and the closed mode. As depicted in the schematic drawing shown in Fig. 1, the input ports of both fingers were mounted on a linear stage that was driven by a stepper motor (Oriental Motor PKP235D23A). The stepper motor was connected to a timing belt-pulley set and a threaded rod. The fixed ports of both fingers were mounted on the main structure of the gripper. The open and closed modes corresponded to the conditions under which the linear stage was driven towards the upper and lower fixed stages, respectively.

To investigate the adaptability of this soft robotic gripper, tests were conducted in order to assess its performance at grasping circular, rectangular, trapezoidal, and concave objects. The total contact length between the fingers and the object being grasped was used as a measure of the adaptability of the gripper. The results are shown in Fig. 9, with the number below each photo indicating the total contact length between the fingers and the object, which was estimated using the image processing program, ImageJ, and by calculating the number of pixels based on their coordinates. In addition, these results were compared with the test results obtained from the fingers printed with an infill density of 100% and the Festo MultiChoiceGripper fingers [37].

From the results of the adaptability tests, it can be seen that the gripper developed in this study had a longer overall contact length when grasping objects of every shape, so it was more adaptable than the other two designs. Our novel multi-phalange fingers, including both the single and multi-infill density designs, were able to conform to all the shapes of the objects under consideration, in contrast to the Festo fingers which adapted well only to the shape of the circular object. Table IV provided a summary of the testing results for the total contact length ratio of various grippers, utilizing Festo's design as the basis. From Table IV, it can be found that the average total contact length of the multi-infill density design was 15 times that of the Festo's design.

To estimate the maximum load capacities that the two-fingered compliant grippers could achieve, payload tests shown in Fig. 10 were conducted. These experiments involved gradually increasing the weight of the mass on the tray hung from a hollow aluminum cylinder with a diameter of 76.1 mm, which was gripped by the two-fingered grippers. The payload test

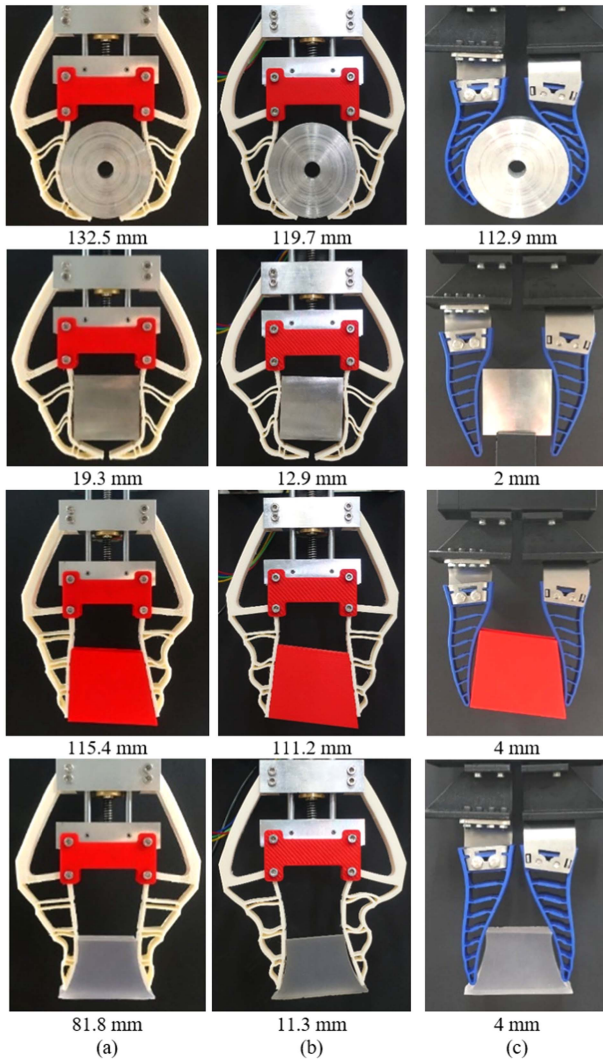


Fig. 9. Adaptability tests for grippers to grasp circular, rectangular, trapezoidal, and concave objects. The number below each photo indicates the total contact length between the fingers and the object. (a) Multi-infill density fingers. (b) Fingers printed with an infill density of 100%. (c) Commercially used Festo MultiChoiceGripper.

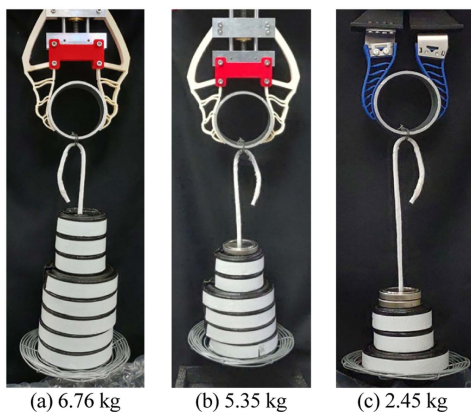


Fig. 10. Payload tests. (a) Multi-infill density fingers. (b) Fingers printed with an infill density of 100%. (c) Festo MultiChoiceGripper.



Fig. 11. Test results for grasping a variety of different objects using the highly self-adaptive gripper with the multi-infill density fingers.

results showed that the grippers using the multi-infill density fingers, the fingers printed with a single infill density of 100%, and Festo's Fin-Ray fingers had maximum load capacities of 6.76 kg, 5.35 kg, and 2.45 kg, respectively. The experimental results showed that the gripper using the multi-infill density fingers had the largest load capacity among the three grippers and the maximum payload was 2.8 times that of the Festo's gripper.

The results demonstrated that the overall designs of our grippers are comparatively adaptive and have a larger load capacity. However, due to the differences in materials, friction coefficients, actuation methods, and motor power between our designs and Festo's design, the comparisons may not be entirely fair. To further demonstrate the capabilities of our highly self-adaptive gripper, tests were conducted using the multi-infill density fingers to grasp a variety of different objects, as shown in Fig. 11. The objects used included three different 3D-printed, irregularly shaped, asymmetrical objects, a 3D-printed concave object, a curved mug, an apple, a raw egg, a mango, a gear, a balloon, a thin plate, and a wide object. The wide object has a width of 128 mm, which is approximately 88% of the maximum fingertip distance, and it is the largest size that can be gripped. The experimental results showed that the gripper proved to be highly adaptable when handling these irregularly shaped objects.

VII. CONCLUSION

This article presented an innovative self-adaptive gripper with two identical multi-phalange, multi-infill density, compliant fingers that proved capable of conforming to irregularly shaped objects. The experimental results demonstrated that this gripper benefitted from a design based on the multi-material topology optimization method and utilized the multi-phalange design connected by flexure hinges. Additionally, the finger with multiple

infill densities required less input force and produced greater output displacement than the fingers with single infill densities of similar weight.

The adaptability of the gripper was determined based on the total contact length between the fingers and the object being grasped. Adaptability tests were conducted with objects of four different shapes, including circular, rectangular, trapezoidal, and concave. The results showed that the adaptability of our novel multi-phalange grippers exceeded that of the Festo MultiChoice-Gripper. Our grippers were able to conform to all four shapes, while the Fin Ray finger design (Festo gripper) could only conform to the circular object. As the contact length increased, the maximum load capacity also increased. Finally, the payload test showed that our gripper has a maximum load capacity of 6.76 kg, offering a solution to the low payload capacity problem found in many soft robotic grippers. The results of the grasping tests demonstrated that our highly self-adaptive gripper can handle circular, rectangular, trapezoidal, concave, asymmetric, deformable, thin, delicate, and fragile objects. Overall, the results of this study suggest that our highly self-adaptive gripper is a good option for applications dealing with unknown objects that may be irregular in size and shape.

REFERENCES

- [1] J. Shintake, V. Cacucciolo, D. Floreano, and H. Shea, "Soft robotic grippers," *Adv. Mater.*, vol. 30, no. 29, 2018, Art. no. 1707035.
- [2] J. Zhou, S. Chen, and Z. Wang, "A soft-robotic gripper with enhanced object adaptation and grasping reliability," *IEEE Robot. Automat. Lett.*, vol. 2, no. 4, pp. 2287–2293, Oct. 2017, doi: [10.1109/LRA.2017.2716445](https://doi.org/10.1109/LRA.2017.2716445).
- [3] C.-H. Liu et al., "Optimal design of a soft robotic gripper for grasping unknown objects," *Soft Robot.*, vol. 5, no. 4, pp. 452–465, 2018.
- [4] C.-H. Liu, F.-M. Chung, Y. Chen, C.-H. Chiu, and T.-L. Chen, "Optimal design of a motor-driven three-finger soft robotic gripper," *IEEE/ASME Trans. Mechatron.*, vol. 25, no. 4, pp. 1830–1840, Aug. 2020, doi: [10.1109/TMECH.2020.2997743](https://doi.org/10.1109/TMECH.2020.2997743).
- [5] H. Zhu et al., "Weight imprinting classification-based force grasping with a variable-stiffness robotic gripper," *IEEE Trans. Automat. Sci. Eng.*, vol. 19, no. 2, pp. 969–981, Apr. 2022, doi: [10.1109/TASE.2021.3054655](https://doi.org/10.1109/TASE.2021.3054655).
- [6] P. Glick, S. A. Suresh, D. Ruffatto, M. Cutkosky, M. T. Tolley, and A. Parness, "A soft robotic gripper with gecko-inspired adhesive," *IEEE Robot. Automat. Lett.*, vol. 3, no. 2, pp. 903–910, Apr. 2018, doi: [10.1109/LRA.2018.2792688](https://doi.org/10.1109/LRA.2018.2792688).
- [7] J. H. Low et al., "Sensorized reconfigurable soft robotic gripper system for automated food handling," *IEEE/ASME Trans. Mechatron.*, vol. 27, no. 5, pp. 3232–3243, Oct. 2022, doi: [10.1109/TMECH.2021.3110277](https://doi.org/10.1109/TMECH.2021.3110277).
- [8] M. Honarpardaz, M. Tarkian, J. Ölvander, and X. Feng, "Finger design automation for industrial robot grippers: A review," *Robot. Auton. Syst.*, vol. 87, pp. 104–119, 2017.
- [9] R. A. Stavenuiter, L. Birglen, and J. L. Herder, "A planar underactuated grasper with adjustable compliance," *Mechanism Mach. Theory*, vol. 112, pp. 295–306, 2017.
- [10] S. Montambault and C. M. Gosselin, "Analysis of underactuated mechanical grippers," *ASME J. Mech. Des.*, vol. 123, pp. 367–374, 2001.
- [11] M. Doria and L. Birglen, "Design of an underactuated compliant gripper for surgery using nitinol," *J. Med. Devices*, vol. 3, no. 1, pp. 011007, 2009.
- [12] N. Lobontiu, *Compliant Mechanisms: Design of Flexure Hinges*. Boca Raton, FL, USA: CRC Press, 2002.
- [13] J. Guo and K.-M. Lee, *Flexonics For Manufacturing and Robotics: Modeling, Design and Analysis Methods*. Berlin, Germany: Springer, 2018.
- [14] Z. Zhuang et al., "Development of a high-performance cutting device based on hybrid actuation for ultra-precision machining," *Mater. Des.*, vol. 225, pp. 111420, 2023.
- [15] S. Kim, C. Laschi, and B. Trimmer, "Soft robotics: A bioinspired evolution in robotics," *Trends Biotechnol.*, vol. 31, pp. 287–294, 2013.
- [16] K. C. Galloway et al., "Soft robotic grippers for biological sampling on deep reefs," *Soft Robot.*, vol. 3, no. 1, pp. 23–33, 2016.
- [17] S. Licht, E. Collins, M. L. Mendes, and C. Baxter, "Stronger at depth: Jamming grippers as deep sea sampling tools," *Soft Robot.*, vol. 4, no. 4, pp. 305–316, 2017.
- [18] Z. Wang, Y. Torigoe, and S. Hirai, "A prestressed soft gripper: Design, modeling, fabrication, and tests for food handling," *IEEE Robot. Automat. Lett.*, vol. 2, no. 4, pp. 1909–1916, Oct. 2017, doi: [10.1109/LRA.2017.2714141](https://doi.org/10.1109/LRA.2017.2714141).
- [19] Z. Wang, K. Or, and S. Hirai, "A dual-mode soft gripper for food packaging," *Robot. Auton. Syst.*, vol. 125, 2020, Art. no. 103427.
- [20] K.-M. Lee, "Design criteria for developing an automated live-bird transfer system," *IEEE Trans. Robot. Autom.*, vol. 17, no. 4, pp. 483–490, Aug. 2001, doi: [10.1109/70.954760](https://doi.org/10.1109/70.954760).
- [21] K.-M. Lee and C.-H. Liu, "Explicit dynamic finite element analysis of an automated grasping process using highly damped compliant fingers," *Comput. Math. Appl.*, vol. 64, pp. 965–977, 2012.
- [22] A. Gao, Y. Zou, Z. Wang, and H. Liu, "A general friction model of discrete interactions for tendon actuated dexterous manipulators," *J. Mechanisms Robot.*, vol. 9, no. 4, 2017, Art. no. 041019.
- [23] P. Šulc, J. Kopačka, L. Pešek, and V. Bula, "Hyperelastic proportional damping for numerical non-conservative dynamic models of hard rubbers under large deformations," *Int. J. Non-Linear Mechanics*, vol. 137, 2021, Art. no. 103823.
- [24] M. Manti, T. Hassan, G. Passeti, N. D'Elia, C. Laschi, and M. Cianchetti, "A bioinspired soft robotic gripper for adaptable and effective grasping," *Soft Robot.*, vol. 2, no. 3, pp. 107–116, 2015.
- [25] W. Crooks, S. Rozen-Levy, B. Trimmer, C. Rogers, and W. Messner, "Passive gripper inspired by *Manduca sexta* and the Fin Ray Effect," *Int. J. Adv. Robotic Syst.*, vol. 14, no. 4, 2017, Art. no. 1729881417721155.
- [26] X. Shan and L. Birglen, "Modeling and analysis of soft robotic fingers using the Fin Ray Effect," *Int. J. Robot. Res.*, vol. 39, no. 14, pp. 1686–1705, 2020.
- [27] D. Petković, N. D. Pavlović, S. Shamshirband, and N. B. Anuar, "Development of a new type of passively adaptive compliant gripper," *Ind. Robot: Int. J.*, vol. 40, no. 6, pp. 610–623, 2013.
- [28] C.-H. Liu, G.-F. Huang, C.-H. Chiu, and T.-Y. Pai, "Topology synthesis and optimal design of an adaptive compliant gripper to maximize output displacement," *J. Intell. Robot. Syst.*, vol. 90, no. 3/4, pp. 287–304, 2018.
- [29] F. Chen et al., "Topology optimized design, fabrication, and characterization of a soft cable-driven gripper," *IEEE Robot. Automat. Lett.*, vol. 3, no. 3, pp. 2463–2470, Jul. 2018, doi: [10.1109/LRA.2018.2800115](https://doi.org/10.1109/LRA.2018.2800115).
- [30] C.-H. Liu, L. J. Chen, J. C. Chi, and J. Y. Wu, "Topology optimization design and experiment of a soft pneumatic bending actuator for grasping applications," *IEEE Robot. Automat. Lett.*, vol. 7, no. 2, pp. 2086–2093, Apr. 2022, doi: [10.1109/LRA.2022.3142910](https://doi.org/10.1109/LRA.2022.3142910).
- [31] H. Zhang, A. S. Kumar, F. Chen, J. Y. Fuh, and M. Y. Wang, "Topology optimized multimaterial soft fingers for applications on grippers, rehabilitation, and artificial hands," *IEEE/ASME Trans. Mechatron.*, vol. 24, no. 1, pp. 120–131, Feb. 2019, doi: [10.1109/TMECH.2018.2874067](https://doi.org/10.1109/TMECH.2018.2874067).
- [32] C.-H. Liu, C.-H. Chiu, M.-C. Hsu, Y. Chen, and Y.-P. Chiang, "Topology and size-shape optimization of an adaptive compliant gripper with high mechanical advantage for grasping irregular objects," *Robotica*, vol. 37, no. 8, pp. 1383–1400, 2019.
- [33] R. Wang, X. Zhang, B. Zhu, H. Zhang, B. Chen, and H. Wang, "Topology optimization of a cable-driven soft robotic gripper," *Struct. Multidisciplinary Optim.*, vol. 62, pp. 2749–2763, 2020.
- [34] C.-H. Liu, Y. Chen, and S.-Y. Yang, "Topology optimization and prototype of a multimaterial-like compliant finger by varying the infill density in 3D printing," *Soft Robot.*, vol. 9, no. 5, pp. 837–849, 2022.
- [35] W. Wu, W. Hu, G. Qian, H. Liao, X. Xu, and F. Berto, "Mechanical design and multifunctional applications of chiral mechanical metamaterials: A review," *Mater. Des.*, vol. 180, 2019, Art. no. 107950.
- [36] C. Tawk, R. Mutlu, and G. Alici, "A 3D printed modular soft gripper integrated with metamaterials for conformal grasping," *Front. Robot. AI*, vol. 429, 2021, Art. no. 799230.
- [37] [Online]. Available: <https://festo.com/>
- [38] O. Sigmund, "Morphology-based black and white filters for topology optimization," *Struct. Multidisciplinary Optim.*, vol. 33, no. 4–5, pp. 401–424, 2007.
- [39] F. Wang, B. S. Lazarov, and O. Sigmund, "On projection methods, convergence and robust formulations in topology optimization," *Struct. Multidisciplinary Optim.*, vol. 43, no. 6, pp. 767–784, 2011.
- [40] K. Svanberg, "The method of moving asymptotes—A new method for structural optimization," *Int. J. Numer. Methods Eng.*, vol. 24, no. 2, pp. 359–373, 1987.
- [41] O. Sigmund, "Manufacturing tolerant topology optimization," *Acta Mechanica Sinica*, vol. 25, no. 2, pp. 227–239, 2009.
- [42] C.-H. Liu, Y. Chen, and S.-Y. Yang, "Quantification of hyperelastic material parameters for a 3D-printed thermoplastic elastomer with different infill percentages," *Mater. Today Commun.*, vol. 26, 2021, Art. no. 101895.